



# Enabling a high-performance saltwater Al-air battery via ultrasonically driven electrolyte flow

Huiyu Huang, Pengzhan Liu, Qiuxia Ma, Zihao Tang, Mu Wang, Junhui Hu\*

State Key Lab of Mechanics and Control of Mechanical Structures, Nanjing University of Aeronautics and Astronautics, Nanjing 210016, China

## ARTICLE INFO

### Keywords:

Ultrasound  
Al-air battery  
Electrolyte flow  
Saltwater

## ABSTRACT

As an emerging battery technology, the Al-air flow battery (AAFB) exhibits high energy density due to the recycling of electrolytes, thus showing great potential as a type of clean and sustainable energy storage system. Conventionally, it employs an external mechanical pump to recycle the electrolyte. In this work, the saltwater AAFB in which the electrolyte is recycled by the ultrasonic capillary effect (rather than a mechanical pump) and the reaction chamber is agitated by ultrasonic vibration, is proposed and investigated. Our numerical simulations show that a travelling ultrasonic wave in the electrolyte flow system causes the capillary flow and agitation. The experimental results show that the percentage increase of the peak power density (relative to that with static electrolyte) can be up to about 7.5 times of that with the electrolyte flow driven by a mechanical pump, under the same electrolyte flow rate and concentration ( $3.3 \text{ ml min}^{-1}$  and  $3 \text{ M NaCl}$ ). The optimal peak power density, which can be achieved by optimizing the reaction chamber thickness, electrolyte concentration and ultrasonic vibration velocity, is  $43.88 \text{ mW cm}^{-2}$ . This work illustrates that the acoustofluidic method can not only improve the discharge performance of the saltwater AAFB effectively, but also greatly decrease the energy consumption, weight and volume of the electrolyte driving unit of the AAFB. In addition, analyses based on experimental results show that the energy gain of a series/parallel battery system formed by multiple identical cells can be larger than one, if the number of cells in the system is large enough.

## 1. Introduction

With concerns for fossil energy consumption and environmental pollution, the development of renewable clean energy is becoming more and more important, such as solar, wind, and tidal power [1]. However, these renewable clean energy sources are unstable, which brings great challenges to real-world applications. Therefore, it is necessary to develop stable and reliable energy conversion and storage systems. Among various energy storage systems, batteries have huge advantages due to their flexibility and stability [2]. Since the 1990s, lithium-ion batteries (LIBs) have been widely used in portable electronic devices and electric vehicles (EVs) due to their high energy density, low self-discharge rate and long cycle life [3,4]. Nevertheless, LIBs have disadvantages such as high cost, safety problems, etc. Therefore, metal-air flow batteries (MAFBs) are regarded as a type of clean and sustainable energy storage device of next-generation due to their high theoretical energy density, good safety, low cost, and eco-friendliness [5–7]. A MAFB includes the metal anode, electrolyte and air cathode. Oxygen serving as the reactive material for the cathode comes from the air in the

working environment. Hence, the weight of an MAFB can be greatly reduced, and its energy density can be very high, which is much higher than that of LIBs [8]. The theoretical specific energy densities of Li-air flow battery (LAFB), Al-air flow battery (AAFB), and Zn-air flow battery (ZAFB), can reach  $11.6 \text{ kW h kg}^{-1}$ ,  $8.1 \text{ kW h kg}^{-1}$  and  $1.1 \text{ kW h kg}^{-1}$  [9–11], respectively. Among these MAFBs systems, the AAFB is more competitive compared with other MAFBs, because they are safe, lightweight, stable, cost effective, environmentally friendly and easy to source the metal material (Al). Apart from these merits, although AAFBs are usually electrochemically non-rechargeable, the AAFB can be mechanically charged, and it takes only a few minutes to easily replace a new Al electrode [12–14]. Therefore, AAFBs have received widespread attention and been developed rapidly over the recent years.

As an emerging battery technology, the electrolyte flow can remove the reaction by-products and improve the energy efficiency for AAFBs. Therefore, the AAFB has outstanding electrochemical performance such as excellent discharge performance and long cycle life. In general, the electrolyte flow methods can be divided into two categories, i.e., external mechanical pump-assisted driving (such as peristaltic or syringe

\* Corresponding author.

E-mail address: [ejhhu@nuaa.edu.cn](mailto:ejhhu@nuaa.edu.cn) (J. Hu).

<https://doi.org/10.1016/j.ultsonch.2022.106104>

Received 8 May 2022; Received in revised form 24 June 2022; Accepted 26 July 2022

Available online 29 July 2022

1350-4177/© 2022 Published by Elsevier B.V. This is an open access article under the CC BY-NC-ND license (<http://creativecommons.org/licenses/by-nc-nd/4.0/>).

pumps) and paper-based capillary action driving [15,16]. The external mechanical pump-assisted electrolyte flow driving can not only drive the electrolyte flow fast and stably, but also significantly improve the discharge performance of AAFBs. However, the external mechanical pump-assisted electrolyte flow system is only suitable for large AAFBs system due to its bulky and complex structure. To achieve miniaturization and simplification of AAFBs, a paper-based microfluidic Al-air battery is developed and investigated, in which the electrolyte flow is driven via capillary action in the microchannel of the cellulose paper [17,18]. Nevertheless, due to the limited energy storage of electrolytes and short battery-shelf life, the discharge performance of this microfluidics-based AAFB is quite weak.

It is known that the ultrasonic capillary effect can be employed to drive fluid in micro channels [19,20], in which the capillary effect is enhanced by ultrasound. In ultrasonic pumps based on the ultrasonic capillary effect, the ultrasonic vibration may be applied to the inlet of a capillary tube by an ultrasonic transducer [19,20] or directly applied into the micro channels by vibrating walls of the micro channels [21]. Although it has been applied in ultrasonic pumps, mechanism of the ultrasonic capillary effect is still controversial. Proposed mechanisms of the ultrasonic capillary effect include the squeeze film effect [22], acoustic streaming model [23], cavitation model [24–26] and intermolecular force decrease model [21,27,28]. The intermolecular force decrease model was proposed and developed by the authors' research group, which has been capable of qualitatively explaining all of experimental phenomena related to the ultrasonic capillary effect. The major view point of the model is that ultrasound in liquid can decrease the average intermolecular force in a sonicated liquid no matter whether there exists the acoustic cavitation process.

In this work, we have proposed a high-performance saltwater Al-air battery via ultrasonically driving electrolyte flow with decent discharge performance. Ultrasonic capillary effect is utilized in the AAFB to circulate electrolyte, while the ultrasonic wave transmitted into the reaction chamber is used to agitate the electrolyte to promote the oxidation–reduction reaction (ORR) rate. Fig. 1 shows a schematic of the acoustofluidic saltwater Al-air battery. The optimal peak power density, which is achieved by optimizing the reaction chamber thickness, electrolyte concentration and ultrasonic vibration velocity, can reach  $43.88 \text{ mW cm}^{-2}$ . Also, electrolyte driving unit of the ultrasonically driving electrolyte flow system has smaller weight, volume and power consumption. Therefore, the presented ultrasonic method to drive the electrolyte for AAFBs would be competitive. Meanwhile, the ultrasonic electrolyte flowing method would provide a universal tool to the electrolyte flow technique for metal-air flow batteries. To the best of our knowledge, this is the first work in the battery technology, which utilizes ultrasound to drive electrolyte recirculation flow and enhance the discharge performance of battery.

## 2. Experimental section

### 2.1. Material and chemicals

The saltwater was prepared with deionized water produced by a deionized water preparation system (CJL-20-15, Ultrapure Water Co., Ltd.) and analytical pure sodium chloride ( $\geq 99.8\%$ , Sinopharm Chemical Reagent Co., Ltd.). In the experiments, the electrolytes of aqueous NaCl solutions had different concentrations of 1 M, 2 M, 3 M, 4 M, and 5 M. Pure aluminum with a purity of 99.99% was used as the battery anode. The cathode was a gas diffusion layer composed of a catalyst layer (Pt/C) and carbon paper (HCP120 Shanghai Hesen Electric Co., Ltd.). The catalyst suspension was prepared by mixing catalyst powder (40 wt% Pt/C, Johnson Matthey), Nafion solution (5 wt%,  $45 \pm 3 \text{ mg cm}^{-3}$ , DuPont), and ethanol-deionized water solvent (1:1 vol ratio of ethanol to deionized water). The mass ratio of catalyst powder, Nafion solution and ethanol-deionized water solvents was 1:10:40. After about 1 h of sonication (UH600, Shanghai OuHor Machinery Equipment Co., Ltd.), the catalyst suspension was sprayed onto the carbon paper with an overall Pt/C load of  $2 \text{ mg cm}^{-2}$ . Then the carbon paper electrode was dried at  $90^\circ \text{C}$  for 6 h in a drying oven (DHG500-00, Supo Instrument Co., Ltd.). After the carbon electrode was dried, the copper foil used as the current collector, was bonded to the carbon paper with conductive silver paste to link to the external circuit.

### 2.2. Electrochemical measurements

The electrochemical measurement was carried out by an electrochemical workstation (CHI 760E, Shanghai Chenhua Instrument Co., Ltd.) at room temperature ( $298 \pm 2 \text{ K}$ ). Before the measurement data were collected, the acoustofluidic saltwater Al-air battery was activated by conducting multiple cyclic polarization tests until the peak discharge power density became stable, to remove the  $\text{Al}_2\text{O}_3$  film on the anode [16]. The polarization curves were obtained by the potentiostatic measurement method, in which the testing voltage value ranged from 0.8 V to 0 V with a step of 0.1 V. Each measurement lasted for 60 s, and the stable value in the second-half 30 s was averaged to obtain the current value of the battery. During the measurement, the single electrode potential data was also obtained, using reference electrode (Ag/AgCl, Shanghai Chenhua Instrument Co., Ltd.). The cathode was connected to the reference electrode through a Fluke digital multimeter to obtain the single electrode potential. In addition, in order to obtain the impedance of the battery, the electrochemical impedance spectroscopy (EIS) measurement method was used with a testing frequency range from 100 kHz to 0.1 Hz, with the A.C. amplitude was 5 mV at 0.3 V (peak power density voltage). The power density (PD) was calculated by  $PD = P/A$ , where  $P$  is the battery power, and  $A$  is the active electrode area. To

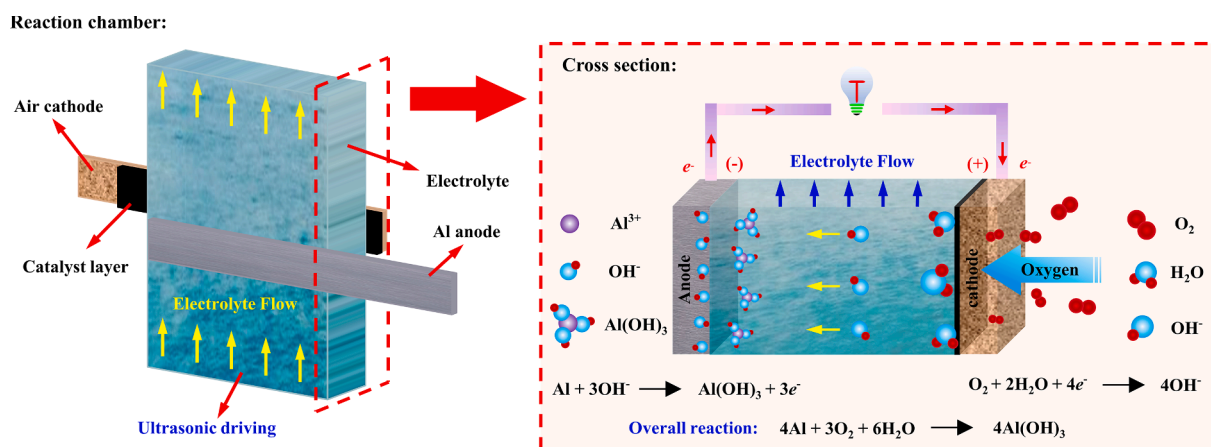


Fig. 1. Schematic of the acoustofluidic saltwater Al-air battery.

investigate the discharge stability and the open-circuit voltage stability of the battery, we conducted discharge experiments under different current densities (1, 10, 20, 40, 60, 80, 100 and 120 mA cm<sup>-2</sup>), in which the discharge duration in each test was 600 s and the total running time of open-circuit voltage stability test was 4800 s. Every experiment was repeated three times.

### 2.3. Battery design and fabrication

Fig. 2(a) shows the structure of the acoustofluidic saltwater Al-air battery proposed and investigated in this work, which is mainly composed of an ultrasonic transducer (HNC-8SH-3840 N, Hainertec Co., Ltd.), a 3 mm-wall-thick poly (methyl methacrylate) (PMMA) electrolyte tank, a capillary glass tube and an Al-air battery. Resonance frequency of the ultrasonic transducer is 40 kHz, and the other performance parameters are listed in Table S1 (Supplementary Materials). As shown in Fig. 2(b), the battery has a sandwich structure, which are composed of two PMMA plates cut by a five-axis vertical machining center (DMU 60 monoBLOCK, DMG) and the middle one is a polyvinyl chloride (PVC) plate cut by a laser precision machining system (ProtoLaser U3, LPKF). To form an electrochemical reaction chamber, a rectangular channel is cut out in the middle plate, with dimensions of 18 mm × 5 mm. The shape of the middle plate is square (30 mm × 30 mm) and a thickness of 3 mm, unless otherwise specified. To dispose the two electrodes, a rectangular cavity is cut out in each PMMA plate. The PMMA plates have identical dimensions of 30 mm × 30 mm × 5 mm, and each electrode reaction area is 0.25 cm<sup>2</sup> (0.5 cm × 0.5 cm). An inlet and outlet are disposed in the anode PMMA plate for the flow of electrolyte. Inside the

cathode PMMA plate, there is an air-breathing window (1 cm × 0.3 cm) for oxygen transport. As shown in Fig. 2(c), the electrolyte tank has a cylinder shape, and its height, inner and outer diameters are 25 mm, 42 mm and 48 mm, respectively. The electrolyte tank's bottom was bonded to a radiation surface of the ultrasonic transducer. The height of the NaCl solutions in the electrolyte tank is 15 mm, and the capillary glass tube is installed perpendicularly to the surface of the vibrating surface, in which the gap between the end of the capillary glass tube and the vibrating surface is 0.01 mm. The outer and inner diameters of the capillary glass tube are 3.0 mm and 1.5 mm, respectively. In this work, when the vibration velocity of the transducer is large enough, the electrolyte can be driven into the capillary glass tube with the ultrasonic capillary effect, as shown in video S1.

### 2.4. Finite element method analyses

To clarify the reason for the ultrasonic effect on the discharge process, the ultrasonic field in the battery was investigated by the finite element method (FEM) (COMSOL Multiphysics software R5.6). In the FEM analyses, a three-dimensional model with the same dimensions and structure as the experimental battery was established. The governing equation for the ultrasonic field in the liquid domain is:

$$\nabla^2 p + \frac{\omega^2}{c^2 + i \frac{\omega}{\rho} \left[ \frac{4}{3} \mu + \mu_B + \frac{(\gamma - 1)k}{C_p} \right]} p = 0 \quad (1)$$

where  $p$  is the acoustic pressure, and  $c$ ,  $\rho$ ,  $\mu$ ,  $\mu_B$ ,  $C_p$ ,  $\gamma$ , and  $k$  are the static sound speed, static density, dynamic viscosity, bulk viscosity, heat

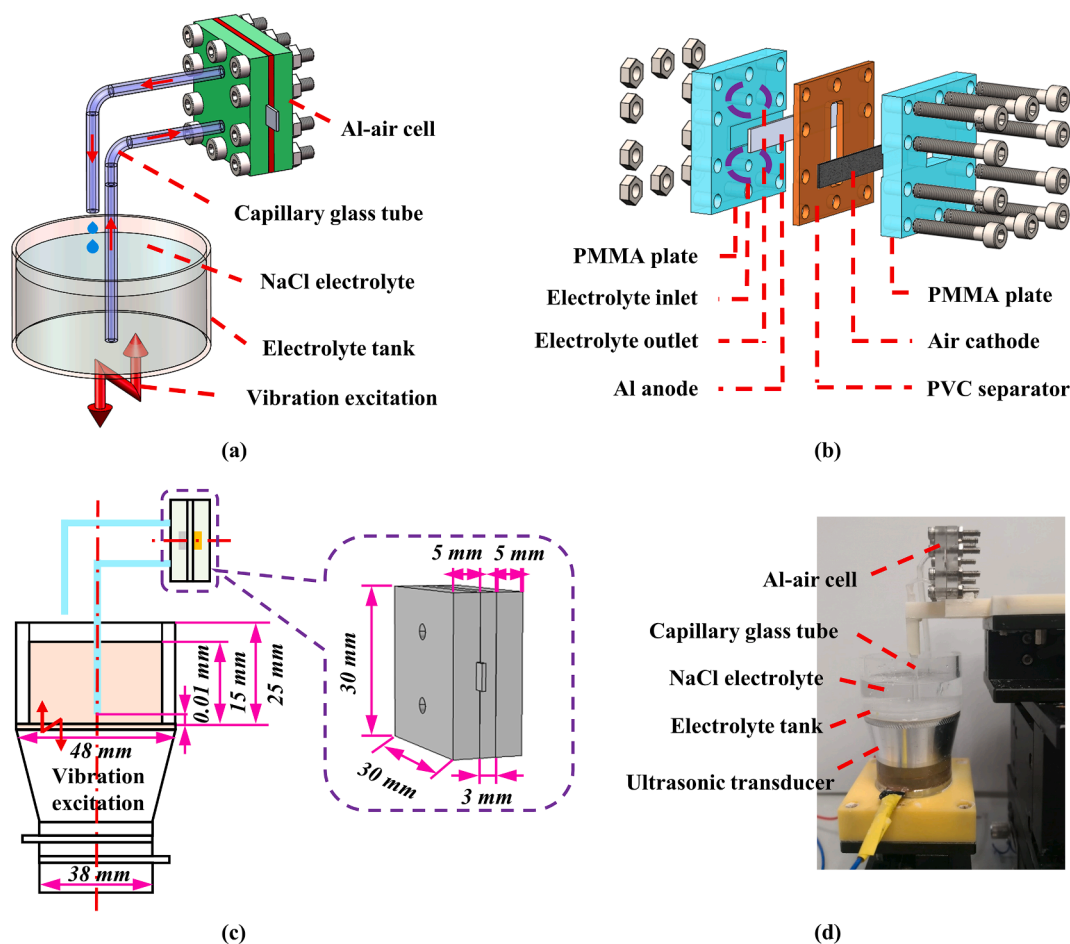


Fig. 2. (a) Structure diagram of the acoustofluidic saltwater Al-air battery. (b) Exploded view of the battery structure. (c) Structure and size of the battery. (d) Photograph.

capacity at constant pressure, ratio of specific heats, and thermal conductivity of the liquid, respectively. The property constants of the materials in the battery system used in FEM computation are listed in Table S2.

The interface between the air and liquid was set to be an acoustically soft boundary, and those between the electrolyte and glass tube/electrolyte tank/reaction chamber were set to be acoustically hard boundaries. At the interface between the transducer radiation face and electrolyte tank, the acoustic-solid boundary was employed, and at the outlet of the glass tube, a perfectly matched layer (PML) was employed.

In the FEM analyses, the working frequency and driving voltage used were 39.7 kHz and 36.8  $V_{0-p}$ , respectively. The free tetrahedron elements were used to mesh the whole structure, and the maximum element size in the fluid domain was 1 mm, which was about 2.65 % of the ultrasonic wavelength  $\lambda$  ( $\lambda = c/f \approx 37.78$  mm, where  $c = 1500$  m/s is the sound speed in the saltwater, and  $f$  is the working frequency).

### 3. Results and discussion

In this work, the discharge performance of the saltwater Al-air battery with the electrolyte flow driven by ultrasound was measured. For comparison, those of the same saltwater Al-air battery but with static electrolyte and electrolyte flow driven by a mechanical pump (LM60A-YZ1515X-6B, Nanjing Runze Fluid Control Equipment Co., Ltd.) were also measured. The mechanical pump has an apparent size of 206 mm  $\times$  143 mm  $\times$  199 mm, and a weight of 3.5 kg, whereas the ultrasonic transducer used in the work has a top diameter of 48 mm, bottom diameter of 38 mm, height of 45 mm, and weight of 0.3 kg, respectively. Thus, the ultrasonic transducer is much smaller and lighter than the mechanical pump. Unless otherwise specified, the experimental conditions are as follows: The working point of the ultrasonic system was at the resonance frequency of 39.7 kHz; The working current voltage were 70 mA (rms) and 26 V (rms), respectively. Flow rate of ultrasonic capillary effect and mechanical pumping was 3.3 ml min<sup>-1</sup>. In addition, all comparison was made with identical electrolyte flow rate values.

#### 3.1. Performance improvement by the ultrasonic driving method

The polarization and power density curves of the saltwater Al-air battery with ultrasonically driven electrolyte flow were measured by using the potentiostatic measurement method with 3 M NaCl electrolytes and electrolyte flow rate of 3.3 ml min<sup>-1</sup>, and the result is shown in Fig. 3(a). It was found that compared with the static electrolyte, both short-circuit current density and peak power density could be increased by the ultrasonic driven electrolyte flow. For the mechanical pumping method, the short-circuit density slightly increases from 121.08 mA cm<sup>-2</sup> (the static electrolyte) to 127.88 mA cm<sup>-2</sup>, which is 5.62 % higher than that of the static electrolyte method. The peak power density

slightly increases from 18.68 mA cm<sup>-2</sup> (the static electrolyte) to 19.40 mW cm<sup>-2</sup> with an increase percentage of 3.85 %. Nevertheless, the short-circuit density and the peak power density of the acoustofluidic saltwater Al-air battery system dramatically increase to 155.60 mA cm<sup>-2</sup> and 24.08 mW cm<sup>-2</sup> with percentage increases of 28.51 % and 28.91 % (relative to the static electrolyte battery), respectively. Thus, the percentage increase of peak power density of the acoustofluidic saltwater Al-air battery (relative to that with static electrolyte) can be up to 7.5 times of that with mechanical pumping, under the same electrolyte flow rate of 3.3 ml min<sup>-1</sup>. From Fig. 3(b), it is observed that both anode and cathode sides have less overpotential loss in the acoustofluidic saltwater Al-air battery than that with mechanical pumping. This performance results from the following two processes which are induced by ultrasound. The first one is the recycling of electrolyte inside and outside the reaction chamber, resulting from the ultrasonic capillary effect. Another one is the agitation induced by the ultrasonic field, which can also weaken the concentration polarization [29–31].

The electrochemical impedance spectroscopy (EIS) was also measured under different driving methods with the same electrolyte flow of 3.3 ml min<sup>-1</sup> and under 3 M NaCl concentration, and the results are shown in Fig. 3(c). The equivalent circuit used to fit the EIS plots is shown in the inset, and the equivalent parameters are listed in Table 1. In the equivalent circuits,  $R_s$  represents the solution resistance,  $R_c$  and  $R_a$  represent the polarization resistance values of the cathode and anode, respectively [15,32,33], which include the charge transfer and diffuse layer resistances, and other resistances. Meanwhile, the  $Q_1$  and  $Q_2$  are the constant phase elements of the cathode and anode, respectively [34,35]. The EIS plot is composed of a high frequency semicircle (the larger one) which is caused by the cathode interfacial electrochemical reactions, and a low frequency semicircle (the smaller one) which is caused by the anode interfacial electrochemical reactions [21,28,36]. From Table 1, it is seen that the ultrasonic driving has a better effect on the decrease of polarization resistances than the mechanical pumping. This phenomenon confirms that the electrolyte flow resulting from the ultrasound is not the only cause of the ultrasound induced performance enhancement. The difference of  $R_c$  (or  $R_a$ ) between the ultrasonic driving and mechanical pumping means that there is other ultrasound induced process(es) affecting the polarization resistances. We attribute this difference to the physical effects of ultrasound in the reaction chamber, such as the electrolyte vibration and ultrasound-induced decrease of inter-molecular force in the electrolyte [29,30].

To further understand the mechanisms of ultrasound-induced flow and discharge performance enhancement, distributions of sound pressure and its phase in the capillary glass tube and reaction chamber were computed. Within the computation capability of our workstation (DELL T7610, 128G Memory), we examined the computational result's dependence on the maximum element size, to justify the meshing method. Fig. 4(a) shows the relationship between the average ultrasonic

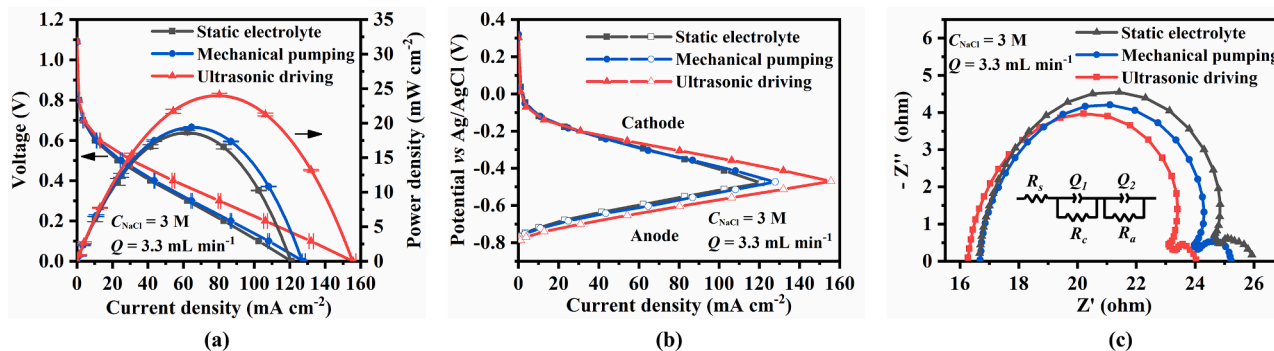
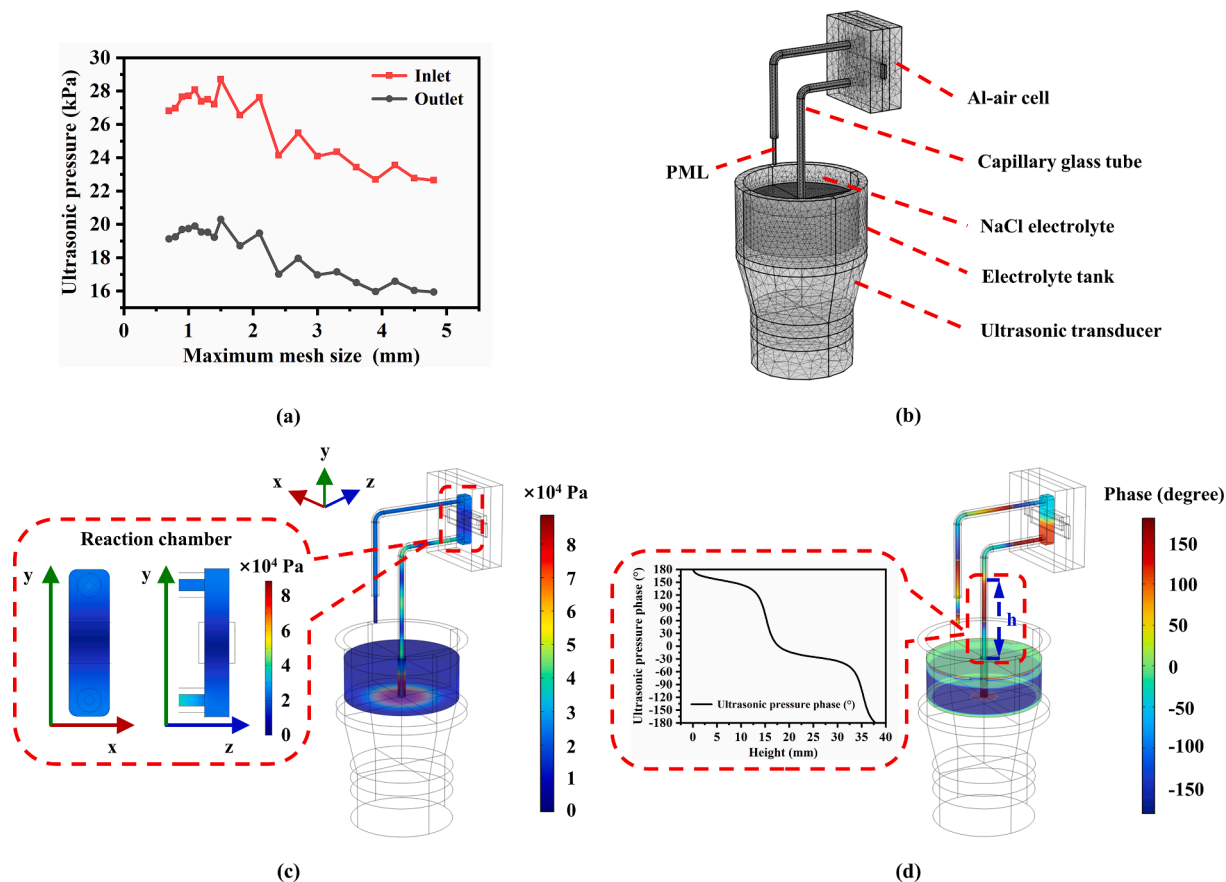


Fig. 3. The electrochemical performance of the saltwater Al-air batteries under different driving methods of electrolyte flow under 3 M NaCl and 3.3 ml min<sup>-1</sup> flow rate. (a) Polarization and power density curves. (b) Single electrode potential curves. (c) Electrochemical impedance spectroscopy (EIS) under different driving methods of electrolyte flow at 3 M NaCl concentration and 3.3 ml min<sup>-1</sup> flow rate.

**Table 1**Fitting parameters of the equivalent circuit for the measured EIS at 3 M NaCl concentration and flow rate of 3.3 ml min<sup>-1</sup>.

Element	$R_s$ ( $\Omega\text{cm}^2$ )	$R_c$ ( $\Omega\text{cm}^2$ )	$R_a$ ( $\Omega\text{cm}^2$ )	$Q_1$ ( $\text{S Sec}^{n_1}\text{cm}^{-2}$ )	$n_1$	$Q_2$ ( $\text{S Sec}^{n_2}\text{cm}^{-2}$ )	$n_2$
Static electrolyte	16.87	8.05	0.67	$7.04 \times 10^{-6}$	1	0.0013	0.87
Mechanical pumping	16.94	7.31	0.65	$5.43 \times 10^{-6}$	0.91	0.0010	1
Ultrasonic driving	16.56	6.80	0.43	$4.81 \times 10^{-6}$	1	0.0012	0.99



**Fig. 4.** Results of FEM analyses: (a) The relationship between the average ultrasonic pressure amplitudes at the inlet and outlet of the capillary tube and the maximum mesh size in the liquid domain. (b) A meshed 3D FEM computation model. (c) The distribution of sound pressure in capillary glass tube and battery. (d) The distribution of sound pressure phase in capillary glass tube and battery.

pressure amplitudes at the inlet and outlet of the capillary tube and the maximum element size in the liquid domain. It is seen that when the maximum element size in the liquid domain decrease to around 1 mm, the average ultrasonic pressure amplitude stops the increase, with a little variation (less than 1 %). Therefore, 1 mm was chosen as the maximum element size in the liquid domain for the mesh construction, under which the total mesh number in the liquid domain was 367419. Under this mesh construction scheme, Fig. 4(b) gives a meshed FEM model of the acoustofluidic saltwater Al-air battery, and Fig. 4(c) & 4(d) show the computed distributions of sound pressure and its phase in the battery system, respectively. Fig. 4(b) confirms that there is ultrasonic field in the capillary tube and reaction chamber. Fig. 4(c) shows that the sound pressure phase in the capillary glass tube decreases as the distance from the tube's inlet increases, which indicates that there is a travelling wave transmitting from the capillary tube's inlet to the reaction chamber. An animation of the computed sound pressure field can be found in Video S2. The travelling wave in the capillary glass tube causes the NaCl solution to flow upward in its length direction due to the decreased intermolecular force [37–39].

### 3.2. Effect of NaCl electrolyte concentration

Increasing the concentration of an electrolyte will improve its conductivity and increase its viscosity, and thus affect the battery performance. The battery performance under different NaCl electrolyte concentrations with the ultrasonic driving method was further investigated, and the results are shown in Fig. 5(a). It is seen that increasing the NaCl concentration from 1 M to 4 M, the peak power density of the battery increases from 12.00 mW cm<sup>-2</sup> to 26.24 mW cm<sup>-2</sup>, and the short-circuit current density increases from 98.40 mA cm<sup>-2</sup> to 159.88 mA cm<sup>-2</sup>. This indicates that in this concentration range, the effect of the conductivity improvement is larger than that of the viscosity increase [16]. However, further increasing the electrolyte concentration to 5 M only slightly improves the performance of Al-air battery. This means that in this concentration range, the effect of the viscosity increase becomes stronger, and the effect of the conductivity improvement is offset. In other words, a too high electrolyte concentration hinders the transportation of the hydroxide ions (OH<sup>-</sup>) towards the anode, which leads to a limited electrode reaction rate [16,40,41]. Fig. 5(b) shows the measured single-electrode potential versus current density at different

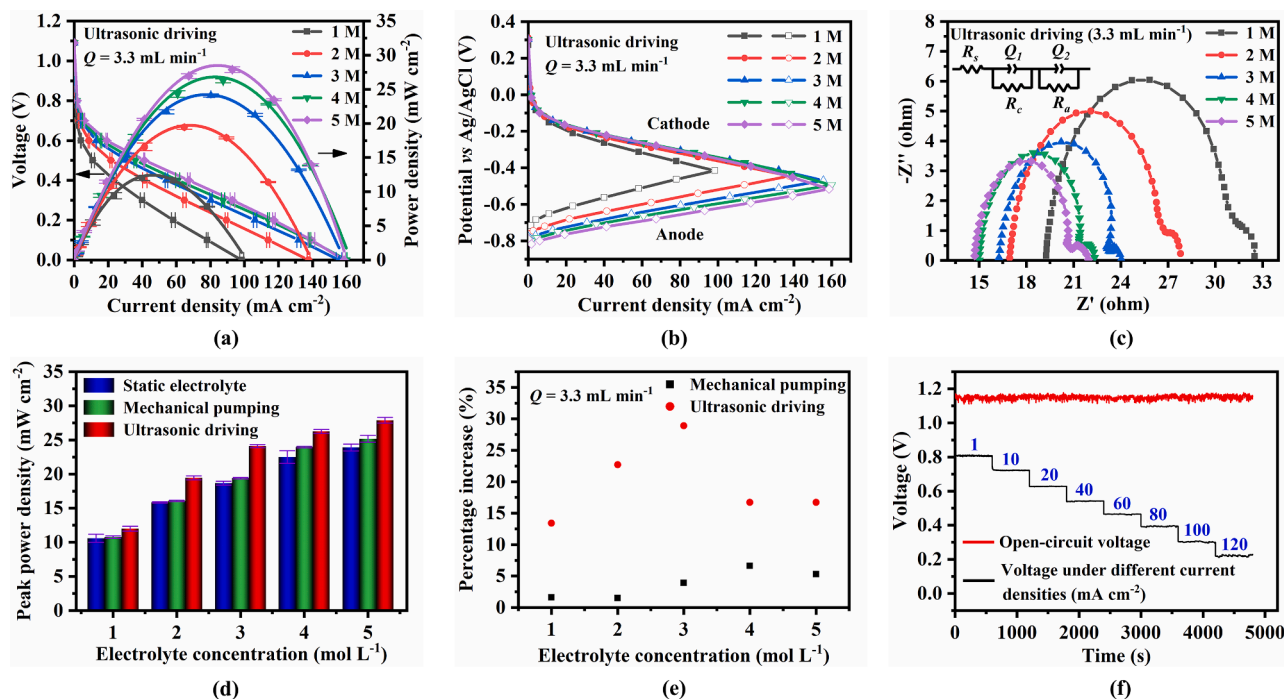


**Fig. 5.** The electrochemical performance of the acoustofluidic saltwater Al-air battery under different NaCl concentrations and  $3.3 \text{ ml min}^{-1}$  flow rate. (a) Polarization and power density curves. (b) Single electrode potential curves. (c) Electrochemical impedance spectroscopy (EIS). (d) The maximum power density versus electrolyte concentration under different driving methods of electrolyte flow. (e) Percentage increase of the peak power density relative to the static electrolyte battery. (f) Open-circuit voltage curve and long-term discharge under different current densities with 5 M NaCl electrolyte concentration.

electrolyte concentration. As the NaCl concentration increases, the conductivity of electrolyte for  $\text{OH}^-$  becomes better, which enhances the oxidation reaction at the anodic surface and thus lowers the anodic potential. For the same reason, the cathodic potential increases as the NaCl concentration increases from 1 M to 2 M. When the NaCl concentration increases from 2 M to 5 M, the cathodic potential has little change. This is because the electrical double layer polarization becomes stronger as the NaCl concentration increases. The change of single-electrode potentials with the current density in Fig. 5(b) is consistent with the voltage change in Fig. 5(a). The measured EIS in Fig. 5(c) suggests that the EIS of the acoustofluidic saltwater Al-air battery is affected by the electrolyte concentration, just like the traditional MAFBs. Thus, the discharge performance of this battery can be further enhanced by increasing electrolyte concentration. For comparison, the polarization curves and single electrode potential curves at different electrolyte concentrations under the mechanical pumping and static electrolyte methods were also measured, and the results are shown in Fig. S1. Fig. 5(d) summarizes the peak power density versus NaCl electrolyte concentrations under different electrolyte driving methods, which indicates that the ultrasonic method brings in the best peak power density of the three methods at different electrolyte concentrations. Fig. 5(e) shows the percentage increase of the peak power density of the flow batteries with the ultrasonic and mechanical pump methods (relative to the battery with static electrolyte). Under the mechanical pumping method, it only increases by 1.60 %, 1.52 %, 3.85 %, 6.58 % and 5.32 % for different saltwater concentrations, respectively. While under the ultrasonic driving method, it drastically increases by 13.40 %, 22.73 %, 28.91 %, 16.73 % and 16.70 %, respectively.

Furthermore, the stability of discharge performance was tested with the multi-step current discharge method at 5 M NaCl electrolyte solution under the ultrasonic driving method, and the result is shown Fig. 5(f). The open-circuit voltage was measured in a duration of 4800 s, and the voltage at each current density was measured separately in a duration of 600 s. It shows that the open-circuit voltage was kept at 1.15 V with a standard deviation of 0.01 V, which indicates that the open-circuit

voltage is quite stable. When the current density reached is less than  $120 \text{ mA cm}^{-2}$ , the voltage has little fluctuation, which also indicates that the acoustofluidic Al-air battery system has a high discharge stability.

### 3.3. Effect of vibration velocity

In this work, the vibration velocity of radiation surface of the ultrasonic transducer was used to represent the strength of ultrasonic vibration of the battery system. The polarization and power density curves of the battery at different vibration velocities were measured with 5 M NaCl electrolyte, and the result is shown in Fig. 6(a). It is observed that when the vibration velocity increases from  $38.68 \text{ mm s}^{-1}$  to  $55.35 \text{ mm s}^{-1}$ , the peak power density increases from  $24.80 \text{ mW cm}^{-2}$  to  $27.88 \text{ mW cm}^{-2}$ . Fig. 6(b) shows the measured flow rate and computed sound pressure (in the middle of the reaction chamber) versus the vibration velocity. It is seen that the ultrasonic capillary effect starts to appear when the vibration velocity or sound pressure exceeds a critical value, and then becomes stronger as the vibration velocity increases. The former phenomenon is due to the flow resistance of the inner wall of the capillary glass tube, and the latter one is because the increase of sound pressure causes the increase of electrolyte flow rate in the battery system, and enhances the ultrasonic agitation effect in the reaction chamber. In the experiments, the maximum flow rate was  $3.3 \text{ ml min}^{-1}$ , owing to the performance limitation of the transducer-electrolyte tank subsystem. Also, it is worth noting that the battery exhibits the best discharge performance ( $27.88 \text{ mW cm}^{-2}$ ) at the vibration velocity of  $55.35 \text{ mm s}^{-1}$  ( $3.3 \text{ ml min}^{-1}$ ), which is the upper limit of the vibration velocity that the experimental transducer can provide [38,39].

A comparison of the energy consumption and peak power density (PPD) enhancement under the ultrasonic driving and mechanical pumping methods is listed in Table 2. Here, the energy consumption refers to the input electric power of the ultrasonic transducer and mechanical pump, and the PPD enhancement is defined as

$$PPD \text{ enhancement} = (PPD_{u(m)} - PPD_0) / PPD_0 \quad (2)$$

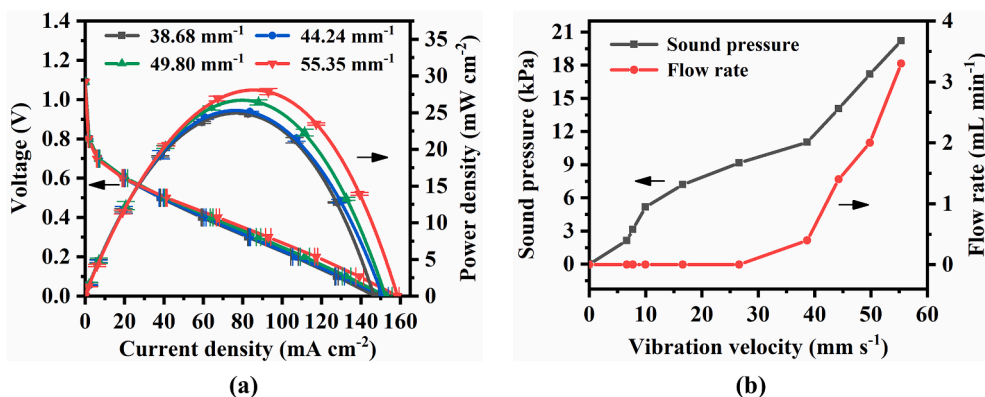


Fig. 6. (a) Polarization and power density curves of the saltwater Al-air batteries under different ultrasonic vibration velocities. (b) Sound pressure in the middle of the reaction chamber and flow rate of ultrasonic capillary effect versus ultrasonic vibration velocity.

Table 2

A comparison of the energy consumption and peak power density (PPD) enhancement under the ultrasonic driving and mechanical pumping methods.

Flow rate (ml min <sup>-1</sup> )	Ultrasonic driving		Mechanical pumping	
	Energy consumption (W)	PPD enhancement (%)	Energy consumption (W)	PPD enhancement (%)
0.4	0.75	3.81	3.12	0.96
1.4	1.06	4.98	3.60	2.97
1.9	1.41	10.51	6.00	3.47
3.3	1.82	16.70	6.48	5.32
Weight and volume of electrolyte driving unit	0.3 kg; 59393 mm <sup>3</sup>		3.5 kg; 5862142 mm <sup>3</sup>	

where  $PPD_{u(m)}$  is the PPD of the saltwater Al-air battery under ultrasonic driving method or mechanical pumping method, and  $PPD_0$  is the PPD of the saltwater Al-air battery with static electrolyte. It is seen that to increase the electrolyte flow rate from 0.4 ml min<sup>-1</sup> to 3.3 ml min<sup>-1</sup>, the energy consumption of the ultrasonic driving and mechanical pumping systems must increase from 0.75 W to 1.82 W, and 3.12 W to 6.48 W, respectively, whereas the PPD enhancement increases from 3.81 % to 16.70 % and 0.96 % to 5.32 %, respectively. Therefore, at the same electrolyte flow rate, the acoustofluidic saltwater AAFB has a better PPD enhancement and lower energy consumption than the conventional AAFB. Moreover, the volume and weight of the ultrasonic transducer are 59393 mm<sup>3</sup> and 0.3 kg, respectively, which are about 1.01 % and 8.57 % of those of the mechanical pump, respectively.

### 3.4. Effect of the reaction chamber thickness

The reaction chamber thickness (distance between the two

electrodes) can also affect the performance of the acoustofluidic saltwater Al-air battery, as indicated by the experimental results in Fig. 7(a). Polyvinyl chloride (PVC) plates with different thicknesses of 0.1 mm, 0.5 mm, 1.0 mm, 2.0 mm and 3.0 mm were used as the electrode spacing separator. Considering the mechanical strength and stability of the AAFB, 0.1 mm was chosen as the minimum thickness of the reaction chamber in this work. It shows that both peak power density and short-circuit current density increase with the decrease of the thickness. As the thickness decreases from 3.0 mm to 0.1 mm, the peak power density increases from 27.88 mW cm<sup>-2</sup> to 43.88 mW cm<sup>-2</sup>, i.e., an increase of 57.39 %. This is because as the reaction chamber thickness decreases, the electrolyte resistance between the two electrodes decreases, and sound pressure in the reaction chamber increases, both of which facilitate the mass transportation [16,32]. Fig. 7(b) summarizes the peak power density at different reaction chamber thickness under the ultrasonic driving, mechanical pumping and static electrolyte methods with a constant NaCl electrolyte concentration of 5 M. At the thickness of 0.1 mm, the peak power density under different driving methods of

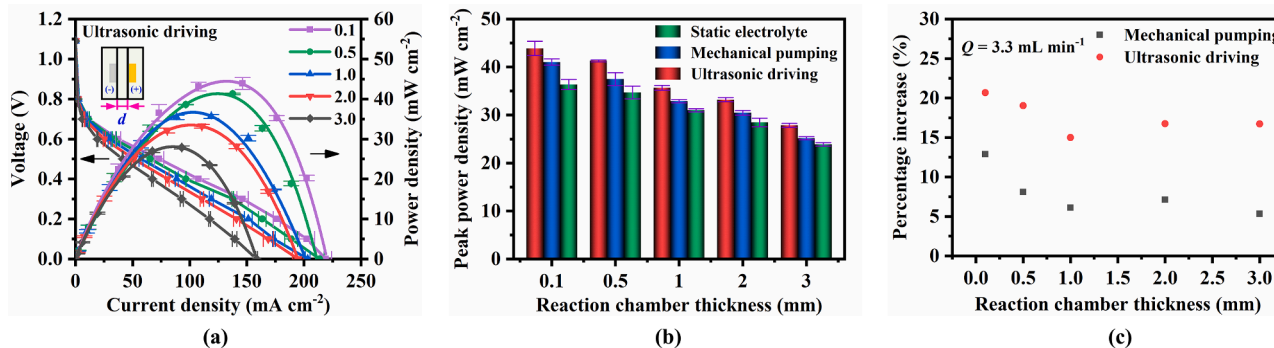


Fig. 7. (a) Polarization and power density curves of the acoustofluidic saltwater Al-air battery for various reaction chamber thicknesses at 5 M NaCl concentration and 3.3 ml min<sup>-1</sup> flow rate. (b) The peak power density of the battery versus reaction chamber thickness for different driving methods of electrolyte flow. (c) The percentage increase of the peak power density under the acoustofluidic and mechanical pumping methods with a reaction chamber thickness of 0.1 mm.

electrolyte flowing decreases in the following order: ultrasonically driving > mechanical pumping > static electrolyte. The polarization and power density curves for the reaction chamber thickness of 0.1 mm, 0.5 mm, 1.0 mm, 2.0 mm and 3.0 mm can be found in Figs. S2. The percentage increase of the peak power density (relative to the static electrolyte) was calculated for the ultrasonic driving and mechanical pumping methods, and the results are shown in Fig. 7(c). By the mechanical pumping method, it is increased by 12.87 %, 8.07 %, 6.10 %, 7.09 % and 5.32 % for the thickness values, respectively, whereas by the

ultrasonic driving method, it is increased by 20.68 %, 19.03 %, 15.00 %, 16.74 % and 16.70 %, respectively. As a conclusion, a smaller reaction chamber thickness is beneficial to increasing the peak power density. According to the experiment results, the peak power density ( $43.88 \text{ mW cm}^{-2}$ ) is the maximum when the reaction chamber thickness is 0.1 mm.

### 3.5. Acoustofluidic saltwater Al-air battery stacks

A single acoustofluidic Al-air cell not only provides a limited output

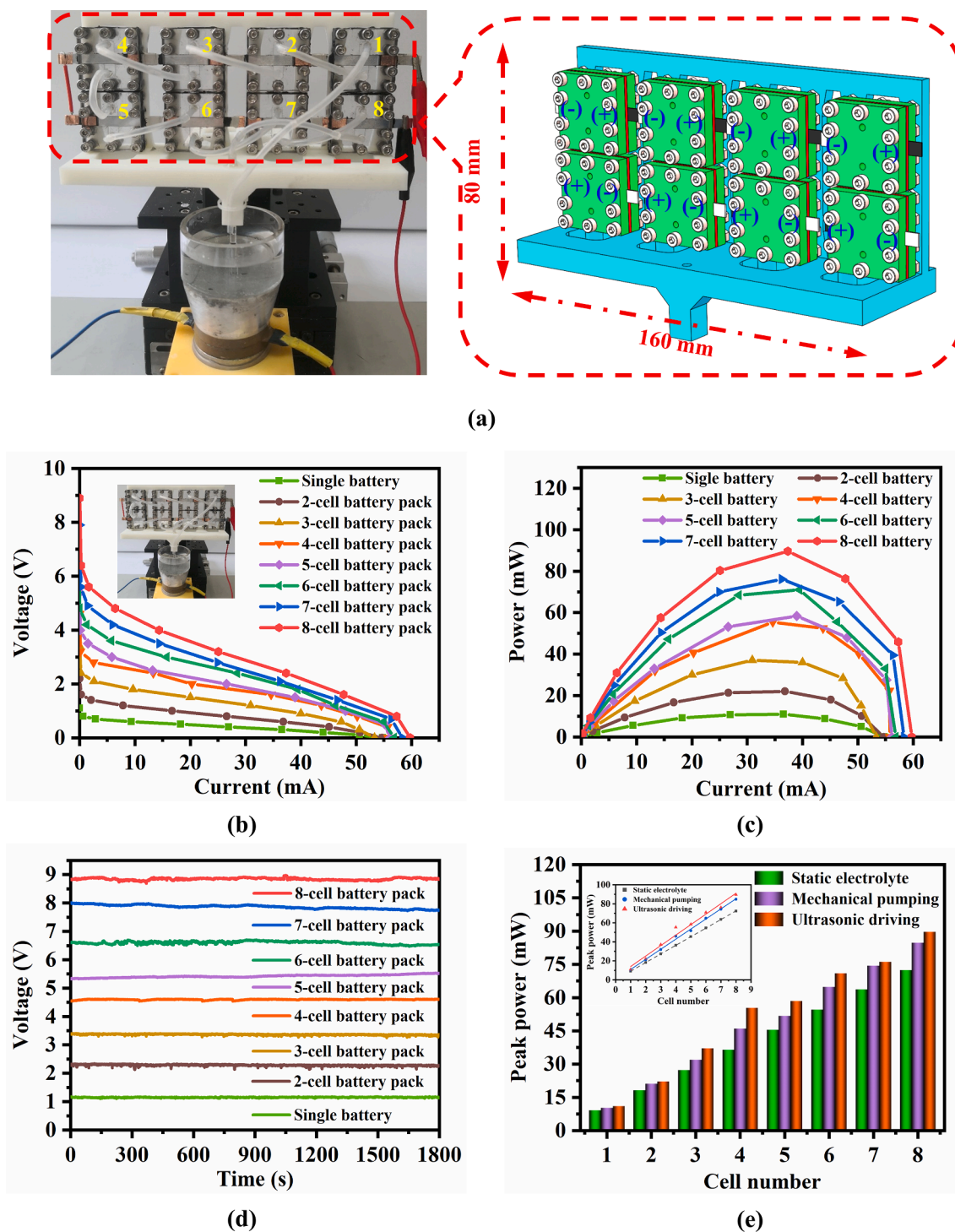


Fig. 8. (a) An 8-series-cell battery pack formed by eight acoustofluidic saltwater Al-air cells connected in series. (b) Polarization ( $j$ - $v$ ) and (c) power curves for 8-series-cell battery packs of acoustofluidic saltwater Al-air batteries with 5 M NaCl,  $3.3 \text{ ml min}^{-1}$  and 0.1 mm reaction chamber thickness. (d) Open-circuit voltage of the cell packs with different cell numbers. (e) The peak power with different cell number.

voltage (V) and peak power (mW), but also limits the utilization rate of ultrasonic energy. To investigate the performance of a battery pack formed by multiple acoustofluidic saltwater Al-air cells, an 8-series-cell battery pack was fabricated, as shown in Fig. 8(a). It is the series of eight identical acoustofluidic saltwater Al-air cells and the capillary rubber tubes for each cell were also in series. The experiments were carried out under the conditions of 5 M NaCl,  $3.3 \text{ ml min}^{-1}$  flow rate and 0.1 mm reaction chamber thickness. From Fig. 8(b) and 8(c), it is seen that the peak power and open circuit voltage of battery packs are almost proportional to the cell number. The peak power of the 8-series-cell battery pack is 89.61 mW, that is, about 8 times of that of the single cell (10.97 mW). From Fig. 8(d), it is known that the open-circuit voltage of the battery pack is approximately proportional to the cell number, that is, it is 8.9 V at a cell number of 8 (open-circuit voltage of a single cell is 1.1 V). Fig. 8(e) shows a comparison of the peak powers of the 8-series-cell battery pack under the ultrasonic driving and mechanical pumping, with the same working conditions. It is seen that the peak power of the battery pack under the ultrasonic driving is higher than that under the mechanical pumping, by 1.2 – 2.1 times.

Although the ultrasound can increase the peak output power of the Al-air saltwater battery, it consumes electrical energy. Thus, whether the ultrasound induced output power increase of the battery can be more than the consumed electric power by the ultrasonic transducer was investigated. To investigate this problem quantitatively, energy gain (EG) of an Al-air saltwater battery system is defined as follows:

$$EG = (P_u - P_0)/P_{in} \quad (3)$$

where  $P_u$  is the peak output power of the saltwater Al-air battery under ultrasonic driving method,  $P_0$  is the peak output power of the saltwater Al-air battery with static electrolyte, and  $P_{in}$  is the input power (power consumption) of the ultrasound transducer. According to the experimental results of the 8-series-cell battery pack, the energy gain of the battery system shown in Fig. 9(a), which is formed by the parallel of multiple identical 8-series-cell battery packs, was simulated. In each battery pack, the electrolyte flow system is in series. Thus, the electrolyte flow system of each battery pack only has one inlet tube which is inserted into the electrolyte tank and one outlet tube which is suspended above the electrolyte tank. The simulated energy gain versus the number of battery packs  $N$  in parallel is shown in Fig. 9(b). It shows that the energy gain becomes larger one when  $N$  is more than 108, which indicates the ultrasound induced increase of peak output power can be more than the electric power consumed by the ultrasonic transducer if the number of battery packs in parallel is more than 108. As the surface area of electrolyte in the tank and the capillary glass tube is  $1385 \text{ mm}^2$  and  $7 \text{ mm}^2$ , respectively, the total cross-sectional area of the inlet capillary glass tubes of the 108 battery packs only shares 54.6 % of the

electrolyte surface area.

If the number of battery cells in each series branch is more than 8, then the line of energy gain in Fig. 9(b) will have a larger slope, and the number of battery packs in parallel to keep  $EG > 1$  will be less. Moreover, the diameter of the electrolyte tank may be designed to be larger than that of the radiation surface of the ultrasonic transducer. In this case, more inlet capillary glass tubes can be inserted into the electrolyte tank, which means a much larger energy gain at the same number of the battery packs.

In addition, one may use a piezoelectric disk working in the thickness vibration mode to excite the electrolyte tank, to decrease the power consumption and increase the energy gain. With this ultrasound excitation method, the volume of the ultrasonic vibration excitation system may be reduced greatly, and the volume power density of the system will be increased greatly.

#### 4. Conclusions

In this work, a novel acoustofluidic saltwater Al-air battery, in which the ultrasonic vibration is employed to drive the electrolyte flow and generate the ultrasonic field in the reaction chamber to enhance the battery performance, has been proposed and investigated. The percentage increase of peak power density relative to that with static electrolyte is up to about 7.5 times of that with the mechanical pumping method, under the electrolyte flow rate of  $3.3 \text{ ml min}^{-1}$  and 3 M NaCl. The optimal peak power density of the acoustofluidic saltwater Al-air battery, which is achieved by optimizing the reaction chamber thickness, electrolyte concentration and ultrasonic vibration velocity, is  $43.88 \text{ mW cm}^{-2}$ . This work provides a new and effective method to increase the peak power of a given saltwater AAFB, while keeping a good stability of its discharge performance. The energy consumption, weight and volume of electrolyte driving unit of the acoustofluidic saltwater AAFB are much less than those of a conventional AAFB. The energy gain of a parallel battery system formed by multiple identical cells can be larger than one, if the number of cells in the system is large enough. We believe that the acoustofluidic saltwater Al-air battery system proposed in the work has potential applications in the energy storage systems that have strict requirements in eco-friendliness, cost effectiveness, safety, and discharge process stability.

#### CRediT authorship contribution statement

**Huiyu Huang:** Conceptualization, Formal analysis, Writing – original draft. **Pengzhan Liu:** Methodology, Writing – review & editing. **Qiuxia Ma:** Formal analysis, Writing – review & editing. **Zihao Tang:** Formal analysis. **Mu Wang:** Formal analysis. **Junhui Hu:**

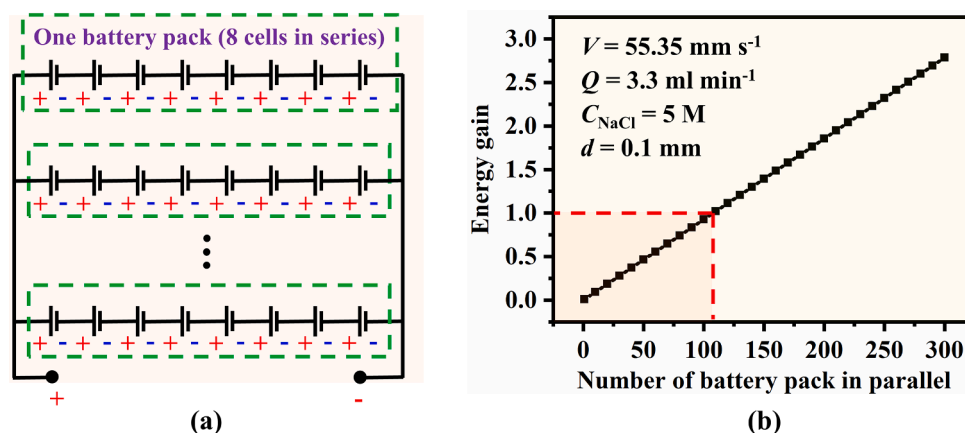


**Fig. 9.** (a) Electric circuit of the Al-air saltwater battery system to achieve an energy gain larger than one. (b) Energy gain versus number of the identical 8-series-cell battery packs in parallel.

Conceptualization, Formal analysis, Funding acquisition, Methodology, Supervision, Writing – review & editing.

### Declaration of Competing Interest

The authors declare that they have no known competing financial interests or personal relationships that could have appeared to influence the work reported in this paper.

### Acknowledgment

This work is supported by the following funding organizations in China: the National Natural Science Foundation of China (Grant No. 11974183) and PAPD.

### Appendix A. Supplementary data

Supplementary data to this article can be found online at <https://doi.org/10.1016/j.ultsonch.2022.106104>.

### References

- [1] S. Chu, A. Majumdar, Opportunities and challenges for a sustainable energy future, *Nature* 488 (2012) 294–303.
- [2] B. Dunn, H. Kamath, J.M. Tarascon, Electrical energy storage for the grid: a battery of choices, *Science* 334 (2011) 928–935.
- [3] Y. Tanaka, H. Okawa, T. Kato, K. Sugawara, Effects of ultrasound irradiation on Au nanoparticles deposition on carbon-coated LiNi<sub>0.5</sub>Mn<sub>1.5</sub>O<sub>4</sub> and its performance as a cathode material for Li ion batteries, *Ultrason. Sonochem.* 82 (2022), 105879.
- [4] Y.C. Feng Jiang, S. Ju, Q. Zhu, L. Zhang, J. Peng, X. Wang, J.D. Miller, Ultrasound-assisted leaching of cobalt and lithium from spent lithium-ion batteries, *Ultrason. Sonochem.* 48 (2018) 88–95.
- [5] X.P. Han, X.P. Li, J. White, C. Zhong, Y.D. Deng, W.B. Hu, T.Y. Ma, Metal-air batteries: from static to flow system, *Adv. Energy Mater.* 8 (2018) 1801396.
- [6] M.A. Rahman, X.J. Wang, C.E. Wen, High energy density metal-air batteries: a review, *J. Electrochem. Soc.* 160 (2013) A1759–A1771.
- [7] W. Yu, W. Shang, P. Tan, B. Chen, Z. Wu, H. Xu, Z. Shao, M. Liu, M. Ni, Toward a new generation of low cost, efficient, and durable metal-air flow batteries, *J. Mater. Chem. A* 7 (2019) 26744–26768.
- [8] X. Zhang, X.G. Wang, Z.J. Xie, Z. Zhou, Recent progress in rechargeable alkali metal-air batteries, *Green Energy Environ.* 1 (2016) 4–17.
- [9] P.A.J.P. Zheng, M. Hendrickson, E.J. Plichta, The theoretical energy densities of dual-electrolytes rechargeable Li-Air and Li-Air flow batteries, *J. Electrochem. Soc.* 158 (2011) A43–A46.
- [10] Z.L. Hejing Wen, J. Qiao, R. Chen, R. Zhao, J. Wu, G. Qiao, J. Yang, High energy efficiency and high power density aluminum-air flow battery, *Int. J. Energy Res.* 44 (2020) 7568–7579.
- [11] M. Wu, G. Zhang, H. Tong, X. Liu, L. Du, N. Chen, J. Wang, T. Sun, T. Regier, S. Sun, Cobalt (II) oxide nanosheets with rich oxygen vacancies as highly efficient bifunctional catalysts for ultra-stable rechargeable Zn-air flow battery, *Nano Energy* 79 (2021), 105409.
- [12] T. Hibino, K. Kobayashi, M. Nagao, An all-solid-state rechargeable aluminum-air battery with a hydroxide ion-conducting Sb(V)-doped SnP<sub>2</sub>O<sub>7</sub> electrolyte, *J. Mater. Chem. A* 1 (2013) 14844–14848.
- [13] Z.J. Xia, Y.F. Zhu, W.F. Zhang, T.R. Hu, T. Chen, J.G. Zhang, Y.N. Liu, H.X. Ma, H. Z. Fang, L.Q. Li, Cobalt ion intercalated MnO<sub>2</sub>/C as air cathode catalyst for rechargeable aluminum-air battery, *J. Alloy. Compd.* 824 (2020), 153950.
- [14] X. Tang, D. Zhou, B. Zhang, S.J. Wang, P. Li, H. Liu, X. Guo, P. Jaumaux, X.C. Gao, Y.Z. Fu, C.Y. Wang, C.S. Wang, G.X. Wang, A universal strategy towards high-energy aqueous multivalent-ion batteries, *Nat. Commun.* 12 (2021) 2857.
- [15] H.J. Wen, Z.S. Liu, J. Qiao, R.H. Chen, R.J. Zhao, J.C. Wu, G.J. Qiao, J.H. Yang, High energy efficiency and high power density aluminum-air flow battery, *Int. J. Energy Res.* 44 (2020) 7568–7579.
- [16] Y.F. Wang, H.Y.H. Kwok, W.D. Pan, H.M. Zhang, X. Lu, D.Y.C. Leung, Parametric study and optimization of a low-cost paper-based Al-air battery with corrosion inhibition ability, *Appl. Energy* 251 (2019), 113342.
- [17] S.G. Prakash Rewatkar, Catalyst-mitigated arrayed aluminum-air origami fuel cell with ink-jet printed custom-porosity cathode, *Energy* 224 (2021), 120017.
- [18] H.K. Yifei Wang, W. Pan, H. Zhang, D.Y.C. Leung, Innovative paper-based Al-air batteries as a low-cost and green energy technology for the miniwatt market, *J. Power Sources* 414 (2019) 278–282.
- [19] O.V. Abramov, *High-Intensity Ultrasonics: Theory and Industrial Applications*, CRC Press, Singapore, 2019.
- [20] T. Hasegawa, D. Koyama, K. Nakamura, S. Ueha, A design of a miniature ultrasonic pump using a bending disk transducer, *J. Electroceram.* 20 (2007) 145–151.
- [21] J.H. Hu, C.L. Tan, W.Y. Hu, Ultrasonic microfluidic transportation based on a twisted bundle of thin metal wires, *Sens. and Actuators A-Phys.* 135 (2007) 811–817.
- [22] M. Biet, F. Giraud, B. Lemaire-Semail, Squeeze film effect for the design of an ultrasonic tactile plate, *IEEE Trans. Ultrason. Ferroelectr. Freq. Control* 54 (2007) 2678–2688.
- [23] Y. Wada, D. Koyama, K. Nakamura, Numerical simulation of compressible fluid flow in an ultrasonic suction pump, *Ultrasonics* 70 (2016) 191–198.
- [24] Y. Wang, T. Li, L.B. Kong, H.H. Hng, P.S. Lee, Gas flow induced by ultrasonic cavitation bubble clouds and surface capillary wave, *IEEE Trans. Ultrason. Ferroelectr. Freq. Control* 61 (2014) 1042–1046.
- [25] N.V. Dezhkunov, T.G. Leighton, Study into correlation between the ultrasonic capillary effect and sonoluminescence, *J. Eng. Phys. Thermophys.* 77 (2004) 53–61.
- [26] T. Li, J. Ma, A piezoelectric acoustic pump: design, mechanism and characterization, *IEEE Int. Ultrason. Sympos. Proc.* (2011) 1723–1726.
- [27] J.H. Hu, N. Li, J.J. Zhou, Controlled adsorption of droplets onto anti-nodes of an ultrasonically vibrating needle, *J. Appl. Phys.* 110 (2011), 054901.
- [28] J.H. Hu, *Ultrasonic Micro/Nano Manipulations*, World Scientific, Singapore, 2014.
- [29] U.K. Zore, S.G. Yedire, N. Pandi, S. Manickam, S.H. Sonawane, A review on recent advances in hydrogen energy, fuel cell, biofuel and fuel refining via ultrasound process intensification, *Ultrason. Sonochem.* 73 (2021), 105536.
- [30] R. Hilton, D. Dornbusch, K. Branson, A. Tekeci, G.J. Suppes, Ultrasonic enhancement of battery diffusion, *Ultrason. Sonochem.* 21 (2014) 901–907.
- [31] K. Kobayashi, A. Chiba, N. Minami, Effects of ultrasound on both electrolytic and electroless nickel depositions, *Ultrasonics* 38 (2000) 676–681.
- [32] B.B. Chen, D.Y.C. Leung, J. Xuan, H.Z. Wang, A mixed-pH dual-electrolyte microfluidic aluminum-air cell with high performance, *Appl. Energy* 185 (2017) 1303–1308.
- [33] Q. Wang, H. Miao, Y.J. Xue, S.S. Sun, S.H. Li, Z.P. Liu, Performances of an Al-0.15 Bi-0.15 Pb-0.035 Ga alloy as an anode for Al-air batteries in neutral and alkaline electrolytes, *RSC Adv.* 7 (2017) 25838–25847.
- [34] L.M. Pan, D.F. Chen, P.C. Pei, S.W. Huang, P. Ren, X. Song, A novel structural design of air cathodes expanding three-phase reaction interfaces for zinc-air batteries, *Appl. Energy* 290 (2021), 116777.
- [35] L. Fan, H.M. Lu, J. Leng, Performance of fine structured aluminum anodes in neutral and alkaline electrolytes for Al-air batteries, *Electrochim. Acta* 165 (2015) 22–28.
- [36] J.B. Wang, J.M. Wang, H.B. Shao, X.T. Chang, L. Wang, J.Q. Zhang, C.N. Cao, The corrosion and electrochemical behavior of pure aluminum in additive-containing alkaline methanol-water mixed solutions, *Mater. Corros.* 60 (4) (2009) 269–273.
- [37] J. Hu, K. Nakamura, S. Ueha, Optimum operation conditions of an ultrasonic motor driving fluid directly, *Jpn. J. Appl. Phys. Part 1 - Regul. Pap. Short Notes Rev. Pap.* 35 (Part 1, No. 5B) (1996) 3289–3294.
- [38] D. Guyomar, N. Aurelle, L. Eyraud, Piezoelectric ceramics nonlinear behavior. Application to langevin transducer, *J. Phys. III* 7 (6) (1997) 1197–1208.
- [39] N. Aurelle, D. Guyomar, C. Richard, P. Gonnard, L. Eyraud, Nonlinear behavior of an ultrasonic transducer, *Ultrasonics* 34 (2-5) (1996) 187–191.
- [40] M. Nestoridi, D. Pletcher, R.J.K. Wood, S. Wang, R.L. Jones, K.R. Stokes, I. Wilcock, The study of aluminum anodes for high power density Al/air batteries with brine electrolytes, *J. Power Sources* 178 (1) (2008) 445–455.
- [41] I. Smoljko, S. Gudic, N. Kuzmanic, M. Kliskic, Electrochemical properties of aluminum anodes for Al/air batteries with aqueous sodium chloride electrolyte, *J. Appl. Electrochem.* 42 (2012) 969–977.